

# MAGNETIC FLUX TRANSPORT AND THE LONG-TERM EVOLUTION OF SOLAR ACTIVE REGIONS

IGNACIO UGARTE-URRA<sup>1</sup>, LISA UPTON<sup>2</sup>, HARRY P. WARREN<sup>3</sup>, AND DAVID H. HATHAWAY<sup>4</sup>

<sup>1</sup>College of Science, George Mason University, 4400 University Drive, Fairfax, VA 22030, USA

<sup>2</sup>Independent Researcher, Broomfield, CO, 80020, USA

<sup>3</sup>Space Science Division, Code 7681, Naval Research Laboratory, Washington, DC 20375, USA and

<sup>4</sup>NASA Ames Research Center, Mail Stop 258-5, Moffett Field, CA 94035, USA

*Draft version October 2, 2018*

## ABSTRACT

With multiple vantage points around the Sun, STEREO and SDO imaging observations provide a unique opportunity to view the solar surface continuously. We use He II 304 Å data from these observatories to isolate and track ten active regions and study their long-term evolution. We find that active regions typically follow a standard pattern of emergence over several days followed by a slower decay that is proportional in time to the peak intensity in the region. Since STEREO does not make direct observations of the magnetic field, we employ a flux-luminosity relationship to infer the total unsigned magnetic flux evolution. To investigate this magnetic flux decay over several rotations we use a surface flux transport model, the *Advective Flux Transport* (AFT) model, that simulates convective flows using a time-varying velocity field and find that the model provides realistic predictions when information about the active region's magnetic field strength and distribution at peak flux is available. Finally, we illustrate how 304 Å images can be used as a proxy for magnetic flux measurements when magnetic field data is not accessible.

## 1. INTRODUCTION

Solar activity is strongly modulated by variations in the Sun's surface magnetic fields. The number of flares and coronal mass ejections, for example, varies in phase with the Sun's 11-year sunspot cycle. Similarly, the magnitude of the Sun's radiative output also changes as the amount of magnetic flux on the solar surface varies. Thus understanding the distribution and evolution of surface magnetic fields is central to discovering the physical mechanisms responsible for the heating of the solar corona and the initiation of coronal mass ejections as well as for developing models that accurately forecast space weather.

The first numerical model of magnetic surface flux transport was developed by DeVore et al. (1984) and during the past several decades there has been considerable progress in simulating the evolution of surface magnetic fields (for reviews see Sheeley 2005; Mackay & Yeates 2012). These models include the effects of differential rotation, supergranular diffusion, meridional flow, and flux emergence and cancellation. Much of this past work has focused on very long time-scales and understanding the transport mechanisms that give rise to the solar cycle. Of particular importance is the role of meridional flow in carrying magnetic flux to the pole where it cancels the existing polar flux and creates the new poloidal field that will seed the next solar cycle.

Our understanding of magnetic flux transport over shorter time scales is, however, much less developed. Because of line-of-sight effects, magnetic observations are generally only reliable while active regions are within a few days of central meridian. With the recent launches of the Solar Terrestrial Relations Observatory (STEREO, Kaiser et al. 2008) and the Solar Dynamics Observatory (SDO, Pesnell et al. 2012), we have a unique opportunity to view the entire solar surface continuously for long periods of time. The twin STEREO spacecraft orbit the Sun at a distance of about 1 AU, but drift away from the earth (in opposite directions) at a rate of about 22° per year. SDO has a geosynchronous orbit that allows for al-

most continuous observations of the Sun from Earth.

In this paper we investigate three questions: [1] How does the total magnetic flux in solar active regions evolve over a period of several solar rotations? [2] Can surface flux transport simulations accurately model this short-term evolution? and [3] What information is necessary to forecast the near-term evolution of solar active regions from far-side observations?

To address these questions we combine STEREO and SDO observations to make 360° maps of the Sun. The absence of magnetographs on the STEREO spacecraft means that we cannot study the evolution of the magnetic field directly with these observations. However, both STEREO and SDO image the Sun in He II 304 Å and we use this channel as a proxy for the total unsigned magnetic flux. As is well known, the radiance in this line is well correlated with the strength of the magnetic field. This is an example of the “flux-luminosity” relationship (e.g., Schrijver 1987).

We isolate and track individual active regions and create continuous light curves for the active regions of interest. We find that the total active region intensity generally follows a similar pattern of emergence over several days followed by a decay with a lifetime proportional to the peak flux in the region. To model this evolution we employ the surface flux transport model recently developed by Upton & Hathaway (2014b,a). This is the first global model to simulate the advection of the magnetic field using a time-varying velocity field instead of an implied diffusion rate. We find that the observed evolution is generally well reproduced by the simulations. Finally, we illustrate how the total flux and geometrical parameters of newly emerged active regions can be estimated from far-side images and embedded in surface flux transport simulations to forecast their near-term evolution. This is an important first step in developing accurate space weather forecasting tools.

## 2. OBSERVATIONS

The STEREO Ahead (A) and Behind (B) spacecraft are, respectively, leading and trailing the Earth in its orbit around

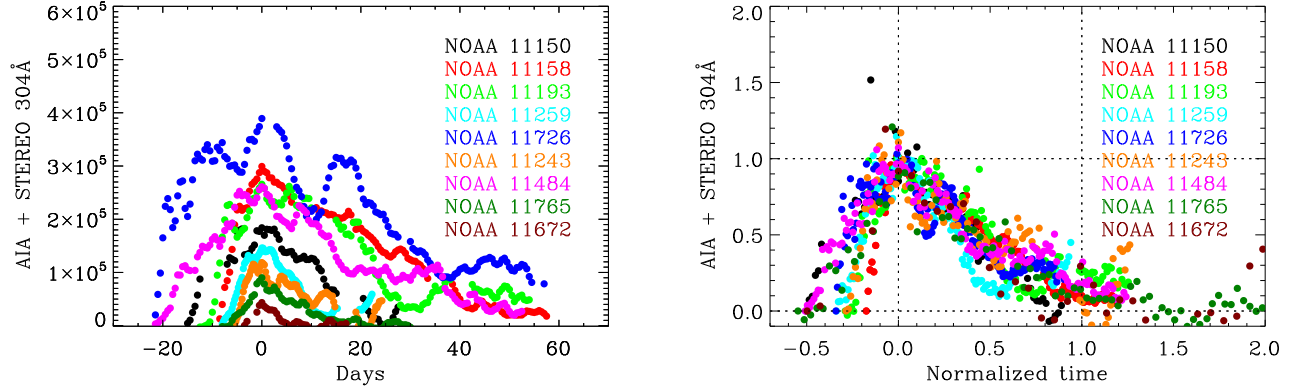


**Figure 1.** 304 Å integrated intensity light curves for the full active region data set. Left panel: light curves have been shifted in time to align their peak intensities to the origin in time. Right panel: light curves have been scaled in intensity to match the peak in NOAA 11158 and then normalized by that peak intensity. The intensity scaling factor is used to scale the times, then normalized by the NOAA 11158 peak-to-disappearance duration.

**Table 1**  
Active region dataset

Number	Latitude	Observing window		Cadence
		Start	End	
11150	-21.5	2011/01/01	2011/02/27	12h
11158	-21.5	2011/02/01	2011/04/18	12h
11193	17.1	2011/04/04	2011/06/14	12h
11243	15.8	2011/06/11	2011/07/25	6h
11259	26.4	2011/07/05	2011/08/13	6h
11272	-13.0	2011/07/28	2011/09/16	6h
11484	12.0	2012/05/07	2012/07/22	12h
11672	-19.3	2013/02/05	2013/02/29	12h
11726	15.0	2013/04/14	2013/07/07	12h
11765	7.9	2013/05/31	2013/07/27	12h

the Sun, providing multiple observational vantage points. We used 304 Å images from EUVI/STEREO (Howard et al. 2008) and AIA/SDO (Lemen et al. 2012) to study the continuous evolution of active regions during their complete lifetimes. For the data set presented here, the separation angle between the two spacecraft and SDO (with the Earth perspective) ranges between 80 – 140°, providing a complete look at the solar surface visible from the ecliptic plane.

The data set (Table 1) consists of 10 active regions manually selected. The criterion for selection was that the evolutionary path (from emergence to growth and maximum development, and to complete decay) was minimally impacted by neighboring active regions. While this is not the most common evolutionary scenario for an active region (because interactions with other regions are frequent) it allows us to study the elemental processes at play in magnetic flux evolution. Still, regions such as 11726, one of the longest-lived, do interact with smaller shorter lived flux concentrations.

To track the history of each individual active region, we made full-Sun Heliographic maps from near-simultaneous 304 Å EUVI (A and B) and AIA images. We chose solar rotation at the latitude of the active region, which conveniently maintains the longitudinal position of the region. Images were processed using standard software provided by the instrument teams. AIA 304 Å images were scaled to EUVI intensities with a time dependent factor available at the SolarSoft STEREO beacon directories. This correction is estimated from the ratio of the median on-disk brightness of EUVI (average of A and B) and AIA hourly images. It is not meant as an absolute calibration correction, but it does remove the

degradation in the AIA 304 Å response with respect to EUVI. The maps were made at a spatial resolution of 1° in longitude and latitude.

Line-of-sight HMI/SDO (Scherrer et al. 2012; Schou et al. 2012) magnetograms were used to compute the total unsigned flux of the active regions as a function of time during their pass along the Earth side view. Both the pixel areas and the observed flux densities were corrected for the line-of-sight projection angle (see Hagenaar 2001).

### 3. RESULTS

#### 3.1. Active region evolution curves

We characterize the evolution of the active regions using 304 Å light curves, which are good indicators of the general trend of emergence, growth, and decay in an active region (e.g. Ugarte-Urra & Warren 2012). The light curves are calculated by integrating the excess counts from a background image in all pixels within a 21° × 21° field-of-view around the center of each region in the Heliographic maps. The background image, which approximates the background of the quiet Sun pre-existent to the active region emergence, is estimated from the median intensity of the bottom 20% intensities in time at each pixel, including times before the emergence. Data is discarded if it lies beyond 0.9 R<sub>⊙</sub> of the center of the EUVI and AIA images to avoid the large interpolation edge effects near the solar limb. Elsewhere a correction is implemented based on a parameterization of the dependence of these effects with longitude at the latitude of interest (see Ugarte-Urra & Warren 2012).

The left panel in Figure 1 shows the light curves of the active regions in the data set with the times of peak in 304 Å intensity co-aligned. The times of peak intensity were determined by smoothing the light curves with a 24h time window, thus minimizing spikes due to transient activity like flares. To take into account different quiet Sun background levels, we have also subtracted the starting intensity from each light curve. The curves reflect the well known evolution of active region magnetic fields with emergence leading to a rapid rising phase followed by a longer decay period. In bipolar active regions, the rise time to maximum development (when emergence ceases) is typically shorter than five days (Harvey 1993), but it can be longer if multiple bipoles are involved and this is the case for some regions in our data set. The decay in most regions in our sample is close to monotonic, but

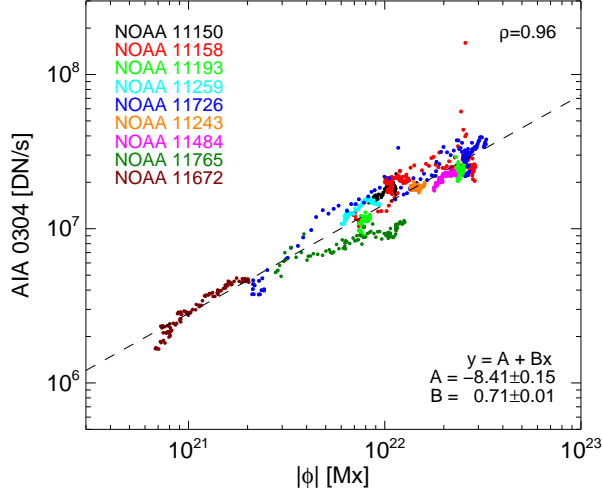


**Figure 2.** Scatter plot of AIA 304 Å counts/s vs. total unsigned magnetic flux.

there are regions, e.g., 11726, that exhibit large variations in 304 Å intensity which are due to interaction with shorter lived nearby flux.

Also evident is that the brighter regions live longer. This is reminiscent of the observed property that active regions with larger fluxes and areas have longer lifetimes (e.g. Mosher 1977). As one will expect intuitively (and we will show quantitatively later in the paper) this is not coincidental, but it has its foundation in the relationship between magnetic flux and 304 Å intensity. An interesting property, that to our knowledge has not been reported before is that the evolution light curves are scalable. In other words, by knowing the peak intensity of a region in 304 Å, one can estimate its lifetime. This is demonstrated on the right panel of Figure 1. In this diagram we show all the light curves scaled to the active region 11158 peak intensity. That same scaling factor is used to scale the time, meaning that an active region twice as bright at peak, will live twice as long. In the figure, intensities have been also normalized by the AR 11158 peak intensity, and the times by the 11158 lifetime, set as the time when the 304 Å intensities reach the flat quiet Sun levels marginally above the original quiet Sun. That plateau is discussed by Sainz Dalda & Martinez Pillet (2008).

To understand the intensity decay, it is important to understand the relationship between the 304 Å maps and the magnetic field because it is the magnetic field evolution on the surface that drives the upper atmosphere response.

### 3.2. Magnetic flux from 304 Å images

The relationship between the X-ray and EUV intensities and magnetic quantities, such as the total unsigned magnetic flux in an active region, has been firmly established (see Gurman et al. 1974; Schrijver 1987; Fisher et al. 1998; Pevtsov et al. 2003; van Driel-Gesztelyi et al. 2003; Fludra & Ireland 2008). Chromospheric EUV lines like He I 584.34 Å are no exception, as shown by CDS/SoHO measurements (Fludra et al. 2002; Fludra & Ireland 2008). We show in Figure 2 that this relationship also holds true for He II 303.8 Å, the dominant spectral line in the 304 Å channel (O’Dwyer et al. 2010).

In Figure 2 we plot the total number of AIA 304 Å counts

per second in an active region as a function of total unsigned flux as measured from HMI magnetograms. The data points represent observations tracking each active region from limb to limb with a cadence of 1 hour. AIA 304 Å images were corrected for the time dependent degradation in sensitivity in the filter response, provided by the instrument team within the standard processing software. A threshold of 85 DN/s/pixel was used to discriminate between the pixels with active region contribution from the quiet Sun pixels. The field-of-view ranged between 215'' – 325'' depending on the size of the region, with the exception of active region 11672 in which we used a 100'' × 110'' area. In the magnetograms, only field strengths above 20 Gauss, in absolute value, were considered.

The power law relationship can be expressed as  $\log(I_{AIA304}) = A + B \log|\phi|$ , where  $I_{AIA304}$  is in DN/s,  $B = 0.71 \pm 0.01$  and  $A = -8.41 \pm 0.15$ . This link between the 304 Å integrated intensity and the magnetic flux is important, not only for its implications in terms of how the EUV emission is generated, as the previous studies have argued, but also because it allows the 304 Å intensity to be used as a proxy of magnetic flux. This is particularly interesting now, as we do not currently have magnetic field measurements from outside the Earth’s line-of-sight perspective, but we do have 304 Å measurements thanks to STEREO. The 304 Å emission is better than other lines at tracking flux evolution. It is formed closer to the solar surface than other EUV and X-ray lines, which extend over larger volumes in the atmosphere and are more sensitive to transient energetic events that generate significant density changes with their respective intensity fluctuations.

This power law can be used to translate the 304 Å light curves in Figure 1 into total unsigned magnetic flux curves for the full lifetime of the active regions. An intermediate step is necessary to go from the integrated intensities of the STEREO heliographic maps to the AIA intensities in the powerlaw. That relationship in our analysis is:  $\log(I_{AIA304}) = C + D \log(I_{HG304})$ , with  $C = -0.9 \pm 0.3$  and  $D = 1.11 \pm 0.04$ .

To assess the importance of the chosen thresholds in the flux-luminosity relationship we repeated the analysis for all regions in different scenarios: AIA thresholds of 5, 85 and 190 DN/s and HMI thresholds of 20, 40 and 80 Gauss. While the slopes of the power law can change significantly in all those permutations due to the added or reduced 304 Å counts and magnetic fluxes, the correlation coefficients are larger than 0.90 in all of them. In the case we selected is  $\rho = 0.96$ . The best fits correspond to an AIA threshold of 85 DN/s with marginal differences in the correlation and fit uncertainties between the 20 (our choice), 40 and 80 Gauss cases. The fit coefficients for the 40 and 80 Gauss cases are respectively  $A = -7.69$ ,  $B = 0.68$  and  $A = -6.83$ ,  $B = 0.64$ .

### 4. THE ADVECTIVE FLUX TRANSPORT MODEL

*Surface Flux Transport* (SFT) describes the latter part of the dynamo process (Babcock 1961), in which the flows on the surface of the Sun transport the magnetic flux from the active region belts to the poles, canceling the previous polar fields during solar maximum and then creating a new poloidal field with the opposite polarity. The strength of this new poloidal field (at solar minimum) is the seed to the next solar cycle (Babcock 1961; Muñoz-Jaramillo et al. 2013).

SFT begins with the emergence of bipolar magnetic active regions with a characteristic polarity and tilt, i.e., with Hale’s polarity and Joy’s Law tilt (Hale et al. 1919; Howard 1991).

The active regions emerge at progressively lower latitudes as the cycle progresses, starting at about  $30^\circ$  and eventually stopping near the equator (Hathaway 2011). The magnetic flux in the active regions is shredded off by turbulent convective motions (over a period of a few days or weeks) and is dispersed into the surrounding plasma.

The flux is then transported by the surface flows: differential rotation, meridional circulation, and the cellular and turbulent motions of convection. The weak magnetic elements are carried to the boundaries of the convective structures (granules and supergranules) by flows within those convective structures, forming a magnetic network. Once concentrated in the magnetic network, the flux is then carried, along with the convective cells, by the axisymmetric differential rotation and meridional circulation.

While the majority of the active region flux will cancel with the opposite polarity from the active region itself or future active regions, some residual flux remnants will remain. The lower latitude leading polarity flux remnants will eventually cancel across the equator, while the higher latitude following polarity flux remnants migrate to the poles. The following polarity flux merges with the original global poloidal field and creates a new poloidal field with opposite polarity, from which the new solar cycle is born.

Most previous SFT models have been highly parametrized, in particular with respect to active region emergence, the meridional flow, and the convective motions. Previous models have been restricted to simulating active region emergence by inserting artificial bipolar active region sources (though some have been based on observed active regions). The adopted meridional flow profiles (sharply peaked at low latitudes, stopping short of the poles, exaggerated variations around active regions) deviate substantially from the observed profiles. Additionally, these models have typically neglected the variability in the meridional flow altogether (the meridional flow is faster at solar cycle minimum and slower at maximum). Furthermore, virtually all previous models have parametrized the turbulent convection by a diffusivity with widely varying values from model to model.

Upton & Hathaway (2014b,a) have developed a new surface flux transport model, the *Advective Flux Transport* (AFT) model. This model is built on the SFT foundation created by DeVore et al. (1984), Sheeley et al. (1985), and Wang et al. (1989). However, while early SFT models were used to probe and help constrain the flows on the Sun, the AFT model was designed with the intent of creating the most realistic SFT model possible by incorporating the observed active regions and surface flows directly, with minimal parametrization.

Upton and Hathaway measured the axisymmetric flows by using feature tracking (Hathaway & Rightmire 2010, 2011; Rightmire-Upton et al. 2012) on full disk images of the Sun's magnetic field obtained from space by the MDI/SoHO (Scherrer et al. 1995) and by the HMI/SDO. The axisymmetric flows were averaged over each 27-day rotation of the Sun and fit with Legendre polynomials. The polynomial coefficients were then smoothed in time and integrated into the model.

The AFT model uses a convective simulation to explicitly model the surface flows produced by the convective flows. The convective simulation, described by Hathaway et al. (2010), uses vector spherical harmonics to create a convective velocity field that reproduces the spectral characteristics of the convective flows observed on the Sun. The spectral coefficients evolve, giving the simulated convective cells finite

lifetimes and moving them with the observed differential rotation and meridional flow. Strong magnetic fields on the Sun inhibit convection; therefore when the flow velocities are employed, they are dampened where the magnetic field is strong. This magnetic field strength dependent effect is difficult to reproduce with the diffusivity used in other models. Advecting the flows with the simulated convection allows the model to surpass the realism that can be obtained by using a diffusivity coefficient.

Magnetic sources can be incorporated in two different ways: either by manually inserting bipolar active regions (e.g., using active region databases like NOAA to insert flux daily as the active region grows) or by assimilating magnetic data directly from magnetograms. This gives the AFT model additional flexibility. While manual insertion allows the AFT model to be used to investigate flows and to make predictions, the assimilation process provides the closest contact to the observations, producing the most accurate synchronic maps of the entire Sun. These maps, referred to as the *Baseline* data set, can be used as a metric for evaluating SFT or as source data for models that extend into the solar atmosphere and the heliosphere.

Upton & Hathaway (2014b) demonstrated the power of their models by simulating Cycle 23 during the polar field reversal. Starting with data 3 years ahead of the reversal, they were able to predict the timing of the field reversal to within four months, with four out of five of their predictions accurate to within a month. Furthermore, they found that their predictions for the polar field evolution stayed in remarkably good agreement with the baseline through to the end of the prediction, an additional 3 years after the reversal, demonstrating the ability to accurately predict the evolution of the Sun's dipolar magnetic field several years in advance.

Upton & Hathaway (2014a) later went on to use their model to simulate most of Cycle 23 and the start of cycle 24 (1997-2013) using RGO and NOAA databases to prescribe active region emergence. They compared the simulated magnetic butterfly diagrams to the baseline and found that despite limited detail in the active region sources (i.e., total flux, tilt, and longitudinal separation), the butterfly diagrams were very similar with distinct features often visible in both. Streams of flux migrating to the poles were also observed, often with a one-to-one correspondence.

The AFT model is unique in several aspects that make it one of the most sophisticated SFT models to date. This model produces the most realistic synchronic full-Sun magnetic maps of the Sun currently available. While the ability of the AFT model to reproduce the evolution of the global magnetic field has been validated on long time scales, its ability to reproduce fine details of active region evolution (e.g., active region decay rate) has yet to be investigated. In fact, Upton & Hathaway (2014a) noted a discrepancy in the amount of flux being injected into the simulated active region model versus the baseline model. This issue is addressed and resolved in Section 5.1.

## 5. MODELING ACTIVE REGION FLUX EVOLUTION

### 5.1. Magnetic flux from the AFT model

While we cannot observe the evolution of the magnetic field when active regions are outside the field-of-view of available magnetometers such as MDI/SoHO or HMI/SDO (both observing from the Earth's perspective), there has been significant progress in recent years in simulating how magnetic field

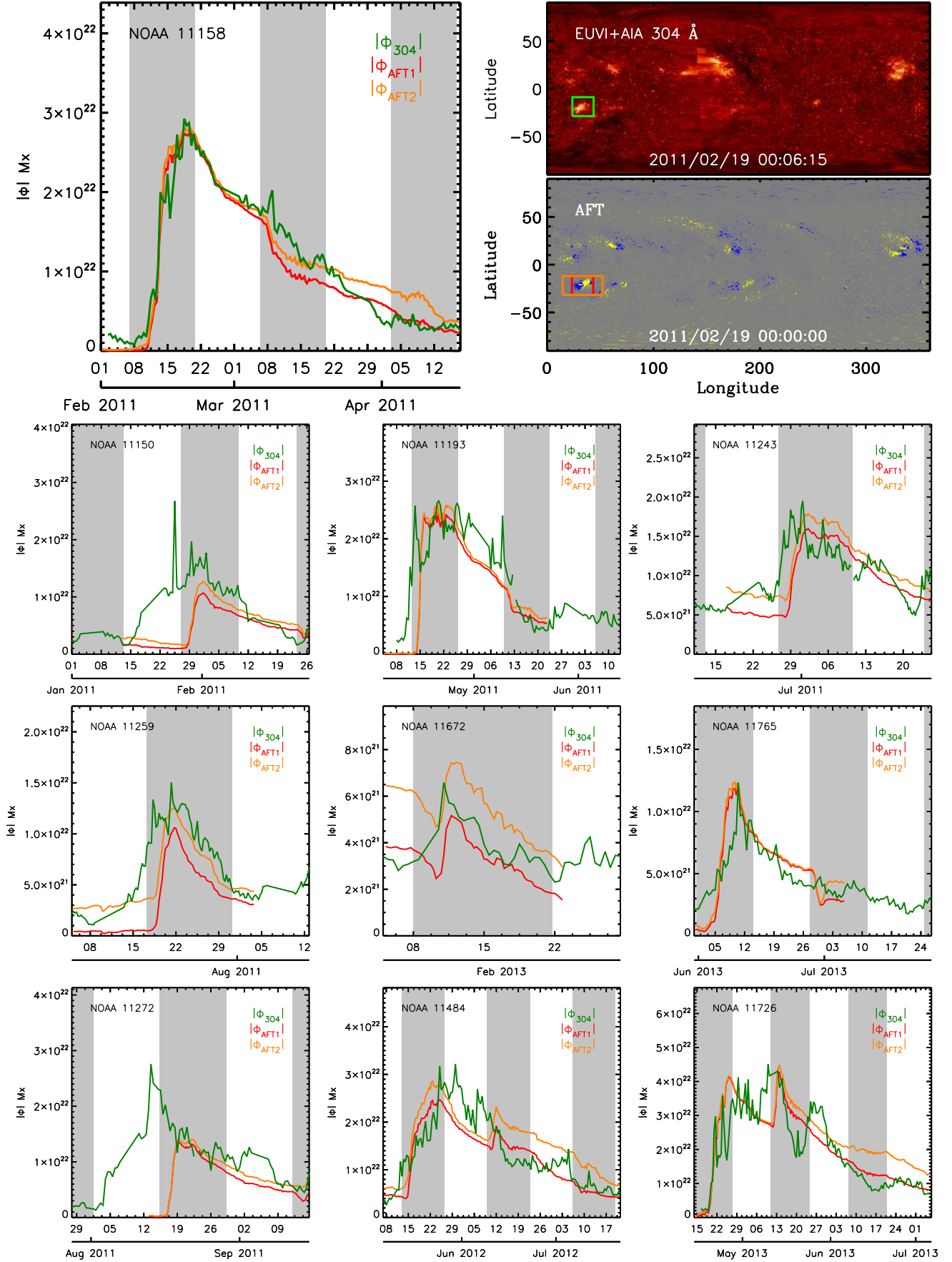


**Figure 3.** Total unsigned magnetic flux of the dataset. Shown in different colors are the flux obtained from the 304 Å proxy (green) and the flux for two area integrations of the AFT model (red and orange) in its standard use, that is including assimilation of HMI magnetograms (i.e., the baseline). Grey areas mark the times when the active region is on the Earth side, when data from HMI magnetograms is being assimilated. 11158 is highlighted on top with the corresponding heliographic and AFT maps near peak 304 Å intensity.



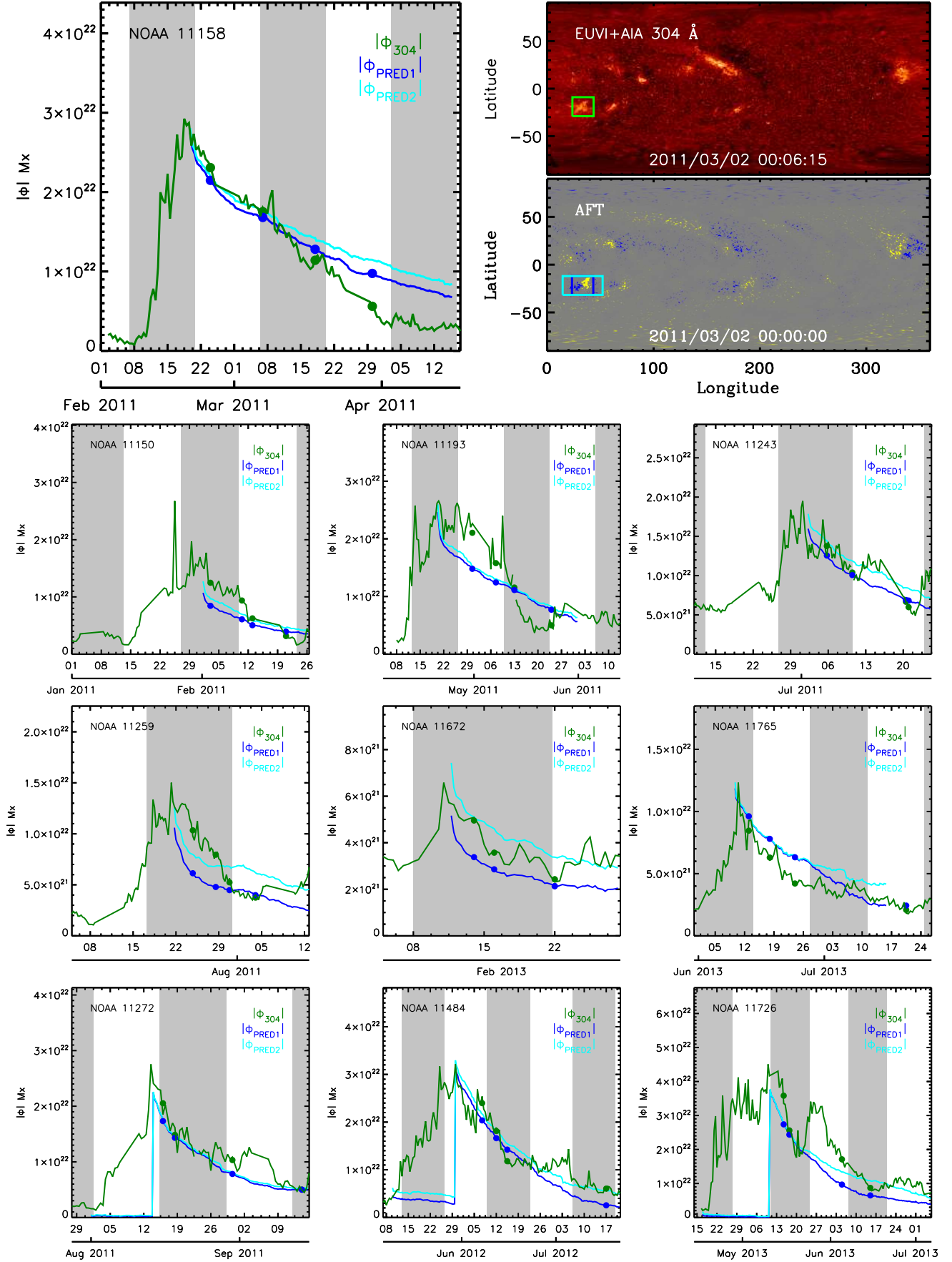


**Figure 4.** Total unsigned magnetic flux as a function of time for the active regions in the dataset. Shown in different colors are the flux obtained from the 304 Å proxy (green) and the flux decay predictions from the AFT model (blue and cyan) in which assimilation has been stopped at the times of peak 304 Å intensity. Grey areas mark the times when the active region is on the Earth side. 11158 is highlighted on top with the heliographic and AFT maps well into the decay phase. Circles correspond to times when  $|\phi_{304}|$  is a fraction (0.8, 0.6, 0.4 and 0.2) of its peak, a reference to Figure 6.

distributions evolve in time. The AFT model is able to evolve observed flux concentrations by simply applying a velocity field that realistically simulates the flows on the photosphere, making it possible to compare observed and simulated magnetic quantities for the complete history of an active region.

The AFT baseline model assimilates magnetic data from HMI magnetograms while the region is on the Earth side. Elsewhere it relies on the prescribed flows to allow the flux concentrations to evolve in time: moving, merging and canceling with other flux concentrations. We investigated the details of the active region evolution in the AFT model by comparing the total unsigned magnetic flux from HMI directly to the total unsigned magnetic flux from the AFT baseline model. It was initially found that the AFT model underestimated the total unsigned magnetic flux, in particular for active regions newly emerged on the western hemisphere. This may explain the flux discrepancy previously noted by Upton & Hathaway (2014a). These comparisons allowed us to make improvements to the original AFT baseline by optimizing the weighting used in the assimilation process such that the baseline total unsigned magnetic flux best matched the observed data, while continuing to mitigate the limb effects seen in the HMI data.

Figure 3 shows comparisons of the total unsigned magnetic flux  $|\phi_{304}|$  inferred from the 304 Å light curves, as described earlier, to the one predicted by the AFT model  $|\phi_{SFT}|$  after integrating the flux density in the SFT maps for absolute values larger than 20 Gauss. The assimilated data is shown by the gray shaded areas in the Figure, while areas with the white background are being evolved solely by the AFT model. The close match of the curves during times of assimilation serves as an assurance that our 304 Å proxy approach works because the AFT model is nearly identical to the real HMI data during this time.

We looked at SFT light curves for two different integration areas, shown with different colors in Figure 3, one matching the field-of-view of the integration area in 304 Å maps, the second one extending that area 25° to the East and West in order to assess the influence of differential rotation on the comparisons. While making the heliographic maps we tuned the rotation rate to the latitude of the region; the maps produced by the SFT model are made at the Carrington rotation rate, thus active regions can rotate out of a fixed longitude. The comparisons reveal that rotation of flux out of the box is not a major source of error. For NOAA 11672, the weakest region, enlarging the area increases the flux because the additional background quiet Sun flux has more weight than in stronger regions.

As illustrated by the 11158 curve, the AFT model can accurately reproduce the active region evolution when the active region is not being observed by HMI and the model is operating without assimilation. Additional flux may emerge, however, while the active region is on the far-side (e.g. 11150, 11272 and 11726). The AFT assimilation process corrects for this new emergence when this flux is observed by HMI and rotates over the East limb. In that respect, the 304 Å proxy is providing information not available to the model.

## 5.2. Forecasting magnetic flux evolution

In the previous sections we established that the peak integrated intensity in 304 Å lightcurves can accurately determine the duration of the decay phase in an active region. We also showed that 304 Å can provide information about magnetic

properties of an active region when magnetic field measurements are not available. Finally and complementary to the others, we have seen that the AFT model has the ability to make these properties evolve realistically in time. The next obvious question that can be raised is: can we combine these three pieces of information to provide predictions about the flux evolution over an active region lifetime?

The answer to the question is affirmative. The importance of the peak 304 Å intensity is that it is directly linked to maximum flux in the region (Figure 2), which coincides with the stoppage of flux emergence. From that moment, the evolution of the flux is fundamentally governed by the diffusive motions of convection, along with the differential rotation and meridional flows (e.g. see review Jiang et al. 2014). Transport by diffusion has been known for many decades (Leighton 1964). In the case of a bipole, it has been shown (Mosher 1977) that the flux decay in one polarity can be expressed as:

$$\phi_+ = \phi_o \operatorname{erf} \left( \frac{a}{\sqrt{4Dt}} \right) \quad (1)$$

where  $\phi_o$  is the initial flux,  $2a$  is the separation between polarities and  $D$  is the diffusion coefficient. The expression illustrates that provided we know the diffusion that affects the field, we only need to know the strength and the separation of the polarities at the start of the process, to predict the decay over time. Simple as this is, however, it is insufficient to fit the slope of the light curves in Figure 1. The limiting factor is that it describes ideal conditions and it does not take into consideration the flux lost under the sensitivity threshold of the instrument or the effect of the convective motions concentrating the magnetic field into the magnetic network. This can be addressed numerically in a model like the AFT model.

In Figure 4, we show comparisons between  $|\phi_{304}|$  and  $|\phi_{SFT}|$  with the restriction that the assimilation of new magnetic field data is stopped when the 304 Å light curve reaches its peak intensity. From that moment onward, the total flux curve is from a field distribution created purely by the modeled transport. The plots show that the AFT model does very well in reproducing the amount of flux decayed over one solar rotation.

In most cases the active region evolution is well matched for the entire period. In cases like 11158, observations and model diverge as the region leaves the Earth view for a second rotation. This may be caused by interactions with nearby flux that has not been assimilated into the model. In fact, two small regions emerged to the East on March 19 and 26, interacted and disappeared, coincidental with drops in the observed total flux. In cases like 11259 and 11672, a rapid decay is observed immediately after the assimilation process is halted. This is likely caused by stochastic differences between the actual and simulated convection patterns. As the active region flux adjusts to the new network pattern, leading and following polarity flux are more prone to interact and cancel with one another. After this brief adjustment period, the decay process stabilizes and mirrors the evolution of the 304 Å flux. We note that this effect may be more pronounced for active regions with a smaller separation distance between the leading and following polarity. For example, while 11259 and 11765 had similar peak intensities, 11765 had about twice separation distance and did not experience a substantial adjustment period. It should also be noted that most of these discrepancies are mitigated by continued assimilation of magnetograms when they are available.

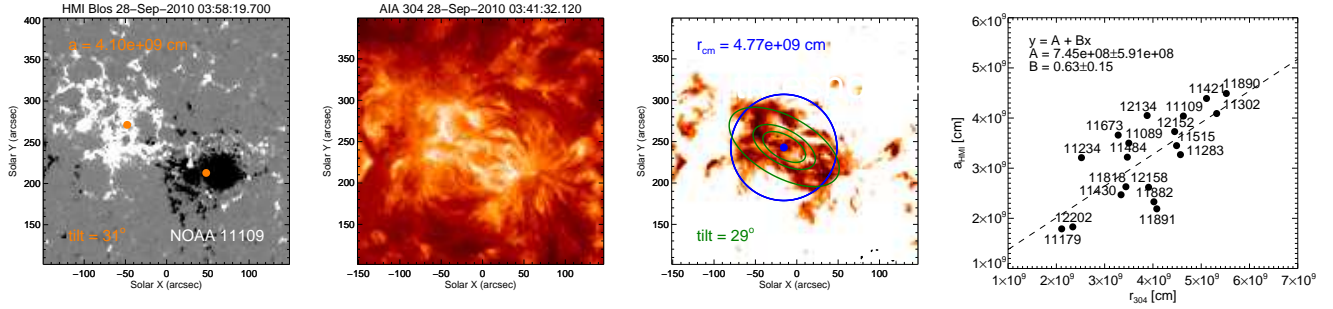


**Figure 5.** The three leftmost panels show a sample case demonstrating the use of 304 Å images to derive properties of the magnetic field distribution. Left panel: HMI magnetogram with polarity centroids, separation ( $2a$ ) and tilt angle. Middle panel: AIA 304 Å image. Right panel: AIA 304 Å image with a threshold of 170 DN/s. The blue circle represents the distance computed from the weighted standard deviation from the 304 Å intensity centroid. The green ellipses correspond to a 2D gaussian fit, which in this example is used to estimate the tilt. The rightmost graph shows this relationship for 19 active regions near central meridian.

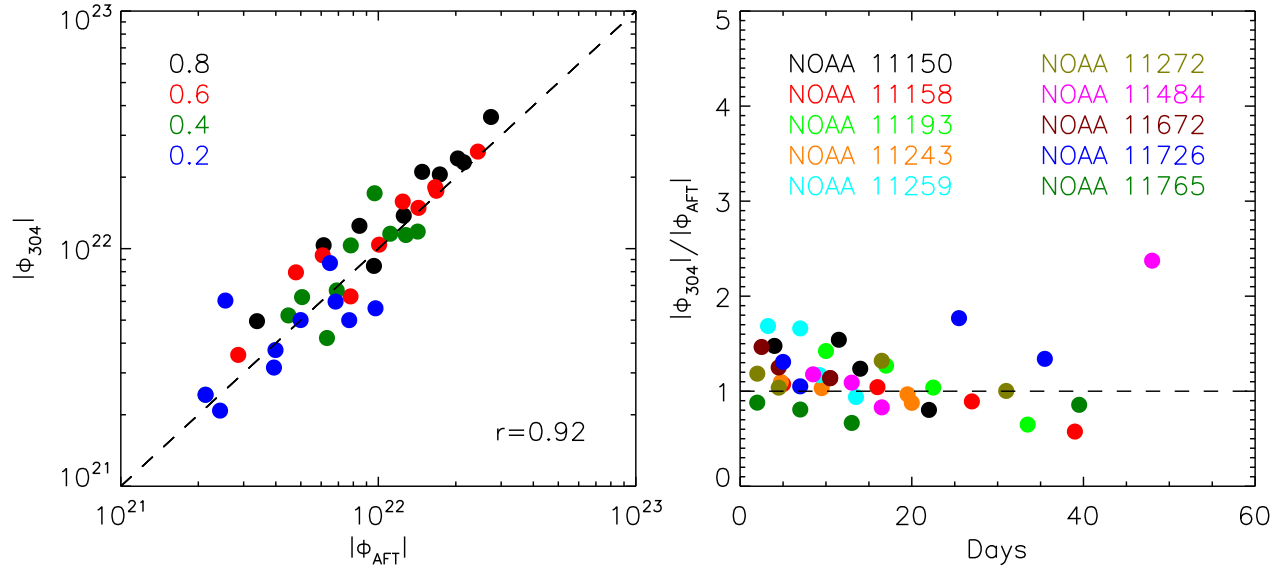


**Figure 6.** Left: Comparison of total unsigned flux for the 304 Å and AFT curves for times when  $|\phi_{304}|$  reaches a fraction of the peak flux. Fractions are denoted by the colors.  $r$  is the Pearson's correlation coefficient. Right: Ratio of both fluxes as a function of time for the same instances. Those times and fluxes are highlighted with circles in Figure 4. Dashed lines indicate expected values for the same flux.

The bottom three panels in Figure 4 (NOAA 11272, 11484 and 11726) are a special subset in the predictions because the peak in 304 Å is reached while on the back side of the Sun and therefore we do not have information about the flux distribution when the decay starts. This makes them excellent cases to test how 304 Å images and light curves serve as the single source of information for a new emergence and its future decay. For these cases, we manually insert a bipolar active region in the AFT maps when the 304 Å has reached its maximum value. In the case of 11484 and 11726, the assimilation is stopped before the actual emergence of the region.

The bipolar strength is chosen from the total unsigned magnetic flux inferred from 304 Å, split between the two polarities. The separation is derived from the weighted standard deviation from the centroid of the 304 Å intensity distribution over a threshold of 170 DN/s. That distance is shown as a blue circle in Figure 5. We determined the relationship between this standard deviation and the distance between polarities for 19 active regions near central meridian and used it to estimate the polarity separation for the three regions with emergences on the back side of the Sun where we only have information about 304 Å. While it is possible in some cases

to also estimate the tilt angle for the two polarities based on a 2D Gaussian fit of the 304 Å intensity distribution (green ellipses in the figure), the method proved unreliable in general without further constraints. The tilt angle ( $\gamma$ ) was, therefore, simply estimated from Joy's law for a given latitude  $L$ ,  $\gamma(L) = 0.51|L| - 0.8^\circ$ . This can be a crude approximation because it is well known that there is a wide scatter around the latitude average (Wang et al. 1989).

How reliable are these predictions? The flux can be consistently predicted within a factor of 2. Figure 6 shows a comparison of 304 Å and SFT fluxes for times when the curves reach a fraction (0.8, 0.6, 0.4 and 0.2) of the peak in the  $|\phi_{304}|$  smoothed light curve. When plotted as a function of time since peak intensity, precision remains rather constant, with only a few points suggesting that it may slowly worsen with time. This does not necessarily imply that the modeling of the flux decay is inaccurate at longer times. Given that many points lie well within that factor of 2 range, it can just be a reflection of the increased chance of other contributions not considered in the model, such as new emergences, affecting the light curves.

These results confirm that, despite the approximations, 304



Å measurements can be sufficient when coupled with a SFT model, to establish how the total unsigned flux of an active region changes over long time scales. Furthermore, a SFT model that combines assimilation of nearside data with far side data from 304 Å measurements should be able to provide a more complete picture of the magnetic field configuration of the entire Sun. This has significant implications for space weather predictions, such as solar irradiance, solar wind, and coronal field models.

## 6. CONCLUSIONS

We present a study of the long term evolution of active regions taking advantage of the full Sun perspective given by the combination of EUVI/STEREO and AIA/SDO images. We find that the 304 Å light curves for isolated active regions of different sizes are scalable by their peak intensities in 304 Å. We show that these 304 Å intensities are directly linked to the total magnetic flux in the regions and use the AFT model to investigate the flux decay over several rotations. We find that the AFT model provides a realistic prediction, within a factor of 2, for the total flux evolution when it is coupled with information about the time of maximum flux in the region. Finally, we show that when magnetic field data is not available, 304 Å images can provide sufficient information about the current stage of active region development to make those predictions plausible. These results can have implications in the exploitation of the data from current and future missions observing the far side of the Sun, and their potential use for predictive science in combination with state-of-the-art magnetic flux transport models. The applicability of this technique needs to be demonstrated in active regions inside large active region complexes, which are frequently observed around the peak of solar activity.

We would like to thank the referee for insightful comments that helped improve the paper. IUU acknowledges funding from the NASA grant NNX13AE06G. HPW's participation was supported by CNR. The SECCHI data are produced by an international consortium of the NRL, LMSAL and NASA GSFC (USA), RAL and U. Bham (UK), MPS (Germany), CSL(Belgium), IOTA and IAS (France). AIA and HMI data are courtesy of NASA/SDO and the AIA and HMI science teams. IUU and HPW would like to thank Neil Sheeley for many helpful conversations. IUU also acknowledges useful comments from William T. Thompson about the EUVI-AIA corrections available in the SolarSoft STEREO beacon directories.

## REFERENCES

- Babcock, H. W. 1961, *ApJ*, 133, 572  
 DeVore, C. R., Boris, J. P., & Sheeley, Jr., N. R. 1984, *Sol. Phys.*, 92, 1  
 Fisher, G. H., Longcope, D. W., Metcalf, T. R., & Pevtsov, A. A. 1998, *ApJ*, 508, 885  
 Fludra, A., & Ireland, J. 2008, *A&A*, 483, 609  
 Fludra, A., Ireland, J., Del Zanna, G., & Thompson, W. T. 2002, *Advances in Space Research*, 29, 361  
 Gurman, J. B., Withbroe, G. L., & Harvey, J. W. 1974, *Sol. Phys.*, 34, 105  
 Hagenaar, H. J. 2001, *ApJ*, 555, 448  
 Hale, G. E., Ellerman, F., Nicholson, S. B., & Joy, A. H. 1919, *ApJ*, 49, 153  
 Harvey, K. L. 1993, PhD thesis, Univ. Utrecht, (1993)  
 Hathaway, D. H. 2011, *Sol. Phys.*, 273, 221  
 Hathaway, D. H., & Rightmire, L. 2010, *Science*, 327, 1350  
 —. 2011, *ApJ*, 729, 80  
 Hathaway, D. H., Williams, P. E., Dela Rosa, K., & Cuntz, M. 2010, *ApJ*, 725, 1082  
 Howard, R. A., et al. 2008, *Space Sci. Rev.*, 136, 67  
 Howard, R. F. 1991, *Sol. Phys.*, 136, 251  
 Jiang, J., Hathaway, D. H., Cameron, R. H., Solanki, S. K., Gizon, L., & Upton, L. 2014, *Space Sci. Rev.*, 186, 491  
 Kaiser, M. L., Kucera, T. A., Davila, J. M., St. Cyr, O. C., Guhathakurta, M., & Christian, E. 2008, *Space Sci. Rev.*, 136, 5  
 Leighton, R. B. 1964, *ApJ*, 140, 1547  
 Lemen, J. R., et al. 2012, *Sol. Phys.*, 275, 17  
 Mackay, D., & Yeates, A. 2012, *Living Reviews in Solar Physics*, 9, 6  
 Mosher, J. M. 1977, PhD thesis, California Institute of Technology, Pasadena.  
 Muñoz-Jaramillo, A., Dasi-Espuig, M., Balmaceda, L. A., & DeLuca, E. E. 2013, *ApJ*, 767, L25  
 O'Dwyer, B., Del Zanna, G., Mason, H. E., Weber, M. A., & Tripathi, D. 2010, *A&A*, 521, A21  
 Pesnell, W. D., Thompson, B. J., & Chamberlin, P. C. 2012, *Sol. Phys.*, 275, 3  
 Pevtsov, A. A., Fisher, G. H., Acton, L. W., Longcope, D. W., Johns-Krull, C. M., Kankelborg, C. C., & Metcalf, T. R. 2003, *ApJ*, 598, 1387  
 Rightmire-Upton, L., Hathaway, D. H., & Kosak, K. 2012, *ApJ*, 761, L14  
 Sainz Dalda, A. S., & Martinez Pillet, V. M. 2008, in *Astronomical Society of the Pacific Conference Series*, Vol. 383, *Subsurface and Atmospheric Influences on Solar Activity*, ed. R. Howe, R. W. Komm, K. S. Balasubramaniam, & G. J. D. Petrie, 115  
 Scherrer, P. H., et al. 1995, *Sol. Phys.*, 162, 129  
 —. 2012, *Sol. Phys.*, 275, 207  
 Schou, J., et al. 2012, *Sol. Phys.*, 275, 229  
 Schrijver, C. J. 1987, *A&A*, 180, 241  
 Sheeley, Jr., N. R. 2005, *Living Reviews in Solar Physics*, 2, 5  
 Sheeley, Jr., N. R., DeVore, C. R., & Boris, J. P. 1985, *Sol. Phys.*, 98, 219  
 Ugarte-Urra, I., & Warren, H. P. 2012, *ApJ*, 761, 21  
 Upton, L., & Hathaway, D. H. 2014a, *ApJ*, 792, 142  
 —. 2014b, *ApJ*, 780, 5  
 van Driel-Gesztelyi, L., Démoulin, P., Mandrini, C. H., Harra, L., & Klimchuk, J. A. 2003, *ApJ*, 586, 579  
 Wang, Y.-M., Nash, A. G., & Sheeley, Jr., N. R. 1989, *Science*, 245, 712